Stark-resonance densities of states, eigenfunctions, and lifetimes for electrons in GaAs/(Al,Ga)As quantum wells under strong electric fields: An optical-potential wave-packet propagation method

Martha L. Zambrano and Julio C. Arce*

Departamento de Química, Universidad del Valle, A.A. 25360, Cali, Colombia
(Received 7 June 2002; published 31 October 2002)

The densities of states, eigenfunctions, and lifetimes of the Stark resonances arising in the conduction band of (Al,Ga)As/GaAs/(Al,Ga)As quantum wells under strong electric fields are determined. A quantitative comparison between the Al-concentration-dependent and -independent effective-mass approximations is also provided. A numerical real-time wave-packet propagation method, successfully implemented earlier for bound states, is adapted for this task by supplementing the Hamiltonian with an exterior optical potential, which damps the wave function in the asymptotic region. Such a technique permits both the reflection-free simulation of the continuum with a finite computational grid and the filtering of the nonresonant background out of the eigenspectrum. This approach yields the entire resonance spectrum of a given structure in a single calculation and L^2 approximations to the continuum eigenfunctions. The lifetime of a resonance is obtained from the time-decay constant of the norm of the calculated L^2 resonance eigenfunction, a method that is applicable to resonances of any line shape.

I. INTRODUCTION

When a quantum system is subjected to a dc field, the formerly discrete quantum states become energy-shifted (metastable) tunneling or above-barrier resonances. In low-dimensional semiconductor heterostructures, this phenomenon is known as the quantum-confined Stark effect (QCSE), which is important for the understanding of their basic physics[1,2] and for their application to the design of optoelectronic devices,[2,3] since these systems are commonly subjected to a voltage bias.

In weak fields (up to about 100 kV/cm), the lowest-lying resonances are so sharp that they are often approximately treated as bound states.[4] In symmetrical structures, within this weak-field regime, the Stark shift is a second-order effect in the perturbation-theory sense.[5] This has motivated the construction of asymmetrical structures, in the hope to achieve first-order energy shifts while still applying weak fields.[6] An obvious alternative for achieving large shifts is to apply strong fields; a regime where, however, perturbation theory fails and significant broadening of the states arises due to the field-induced tunneling,[5,7] specially for excited states. Consequently, it is necessary to devise nonperturbative approaches for the accurate determination of Stark shifts and mean tunneling lifetimes in these systems under strong fields.

The problem of the QCSE has been addressed from both static (spectral) and dynamic perspectives. In static approaches, the energy and lifetime of a resonance are obtained from its peak position and reciprocal full width at half maximum (FWHM), respectively, employing a variety of methods for finding eigensolutions of the time-independent Schrödinger equation (TISE): *Ab initio*,[8] Airy function with real and complex arguments,[9–13] stabilization graph,[14,15] Fourier series,[15] finite difference,[8,16,17] finite element,[18] and complex coordinate.[19] Time-independent numerical finite-difference[8,16,17] and finite-element[18] methods are exact, in the sense that approximations other than a discretization of space and time is not involved, and flexible, since they can deal

with any potential profile; in particular, with any field strength. This makes them particularly useful in cases where analytical methods[9–13] are not applicable and/or other approximate methods[8,14,15,19] are impractical or inaccurate; however, they only yield eigenenergies. On the other hand, in the dynamic perspective the time evolution of a tunneling wave packet is simulated by numerical integration of the time-dependent Schrödinger equation (TDSE).[15–17,20] This provides a dynamical picture of the electron escaping from the well, and the lifetime is often computed from the time-dependent tunneling probability,[15–17] although other alternative prescriptions can be used.[21] Perhaps not surprisingly, the spectral and dynamic *definitions* of the lifetime do not yield similar values (see Sec. IV); accordingly, it is desirable to implement exact numerical methods not only for the calculation of resonance energies but also for the determination of lifetimes within the spectral FWHM definition.

The position dependence of the effective mass is often neglected in both static and dynamic calculations,[9,10,12,14,15] although its importance for the QCSE has been pointed out.[11,13,16] In numerical finite-difference[8,16,17] or finite-element[18] methods, such a dependence can be easily incorporated. In addition, little attention has been devoted to the high-field (say, larger than 200 kV/cm) regime.[10,15]

In this work, the densities of states, eigenfunctions, and lifetimes of all the Stark tunneling resonances arising in the conduction band of $Al_xGa_{1-x}As/GaAs/Al_xGa_{1-x}As$ quantum wells (QW's) under strong electric fields are determined. A quantitative comparison between the Al-concentration-dependent and -independent effective-mass approximations is also provided. A numerical real-time wave-packet propagation method (RTWPM), successfully implemented earlier for bound eigenspectra,[22] is adapted for this task by including in the Hamiltonian an exterior optical potential.[23,24] In this approach, an appropriately chosen test wave packet is numerically propagated in time and its autocorrelation function evaluated. The Fourier transform of such a function yields a continuous spectral density function, which exhibits the weighted densities of states associated with the tunneling and

above-barrier resonances comprised in the test function. Uniform L^2 approximations to the continuum eigenfunctions are obtained by Fourier transforms of the propagated wave packet at the corresponding energies. The optical potential plays two computational roles: simulation of the reflection-free propagation of the wave packet in the continuum, at the same time employing a finite computational grid, and filtering of the nonresonant background out of the test function. The lifetime of a resonance is determined by propagating the corresponding calculated L^2 peak eigenfunction in time and evaluating the decay constant of its norm.[24] When the resonance presents a Lorentzian profile, this procedure yields the same values as the FWHM method,[9–15] although the former is more generally applicable to resonances of any line shape. It must be kept in mind that, although the RTWPM relies on particular solutions of the TDSE, its goal is to extract eigensolutions of the TISE, i.e., it is a time-dependent spectral approach.

This methodology has the same advantages as the aforementioned time-independent numerical methods,[8,16–18] with the additional ones of automatically enforcing the boundary conditions (since the TDSE is an initial-value problem unlike the TISE, which is a boundary-value problem), producing the entire resonance spectrum of a given structure in a single calculation, and yielding Stark shifts, resonance widths, and lifetimes on the same footing. Other wave-packet propagation methodologies, often referred to as equation-of-motion methods, have also proven useful in semiconductor physics for the calculation of the electronic structure of nanoclusters[25] and the optical properties of crystalline and amorphous materials,[26] nanocrystallites,[27] and heterostructures,[28,29] to name a few examples.

In Sec. II, the model for the QW is set up in terms of a position-dependent electron effective mass. Section III presents the general formalism of the RTWPM for the calculation of densities of states, eigenfunctions, and lifetimes for any Hamiltonian that exhibits resonances in its continuum eigenspectrum. In Sec. IV, the strategies employed for the efficient computational implementation of this methodology, in particular, the exterior optical potential, are explained. In Sec. V, the results of the calculations for several well widths and field strengths are presented, discussed, and compared with other reports. Section VI closes with concluding remarks and perspectives for future work.

II. MODEL

In this work, an electron in a symmetrical rectangular QW is considered, with barriers modeled by step functions of height V_0. The structure is subjected to a uniform transverse electric field of strength F, which "tilts" the well as illustrated in Fig. 1. The effective-mass approximation is used, taking into account its dependence on Al concentration.

Employing the well-established BenDaniel-Duke expression for the position-dependent-mass kinetic-energy operator,[16,30] the Hamiltonian takes the form

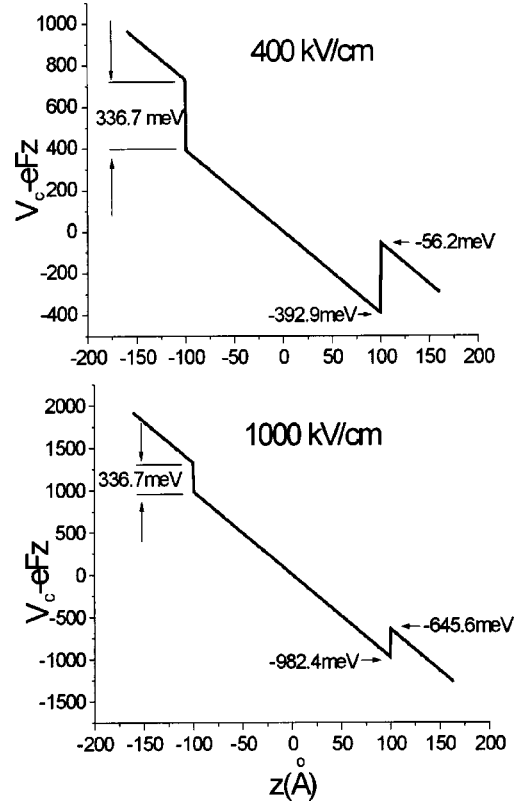$$\hat{H} = -\frac{\hbar^2}{2}\frac{d}{dz}\left(\frac{1}{m_e^*(z)}\frac{d}{dz}\right) + V_C(z) - eFz, \qquad (1)$$

FIG. 1. Conduction-band profiles for a $W = 200$ Å QW under $F = 400$ and 1000 kV/cm.

where $V_C(z)$ is the field-free band-edge potential. This Hamiltonian does not possess bound eigenstates.

III. GENERAL FORMALISM

In the following, it is assumed that the eigenspectrum of the Hamiltonian is fully continuous [like in Eq. (1)], $\hat{H}\varphi_\varepsilon(q) = \varepsilon\varphi_\varepsilon(q)$, where ε is the energy variable, $\varphi_\varepsilon(q)$ is a real, non-L^2, Dirac-delta orthonormalized $[\int \varphi_\varepsilon(q)\varphi_{\varepsilon'}(q)dq = \delta(\varepsilon - \varepsilon')]$ eigenfunction, and q denotes the relevant set of spatial coordinates. Inclusion of a discrete part in the eigenspectrum is straightforward.[22]

On the other hand, it is useful to recall that a resonance embedded in the continuous eigenspectrum of the system can be treated as a discrete, complex, L^2 eigenstate[9–15,19,24,31] of a certain associated non-Hermitian Hamiltonian, $\hat{\tilde{H}}$. The complex energies and "stationary" wave functions are given by

$$E_n = \varepsilon_n - i\Gamma_n/2, \qquad (2)$$

$$\tilde{\Phi}_n(q,t) = \tilde{\varphi}_n(q)\exp(-iE_n t/\hbar), \qquad (3)$$

where ε_n is the (real) energy at the nth resonance peak and $\tilde{\varphi}_n(q)$ is the corresponding complex eigenfunction. Since $\hat{\tilde{H}}$ is not Hermitian, the eigenstates $\tilde{\varphi}_n(q)$ are not necessarily orthogonal, although they can be considered to be approxi-

mately so when the resonance peaks do not overlap significantly. The squared norm of a "stationary" resonance wave function,

$$\langle \tilde{\Phi}_n(t)|\tilde{\Phi}_n(t)\rangle = \exp(-\Gamma_n t/\hbar), \qquad (4)$$

is seen to decay in time with the constant $\Gamma_n/\hbar$, from which the mean lifetime can be defined as

$$\tau_n = \hbar/\Gamma_n. \qquad (5)$$

The aforementioned associated non-Hermitian Hamiltonian can be rigorously constructed by a complex scaling of the coordinates appearing in the Hamiltonian of the system, of the form $q \rightarrow q e^{i\theta}$.[31] The resulting analytically continued Hamiltonian, $\hat{\tilde{H}}(q e^{i\theta}) \equiv \hat{\tilde{H}}_\theta$, exhibits an isolated point spectrum consisting of the discrete complex eigenvalues E_n, accompanied by a continuous spectrum which appears rotated in the complex-energy plane by an angle of -2θ with respect to the (real) spectrum of the original Hamiltonian.[31] Thus, under the complex scaling of $\hat{H}$, the resonance energies and lifetimes are explicitly unraveled and the nonresonant continuum eigenstates acquire a finite lifetime. The same observations about the spectrum hold when the complex scaling is performed only on an exterior contour, instead of on a ray, of the complex-coordinate plane.[32] Such exterior scaling offers the advantageous feature of damping the continuum eigenfunctions in the region of the contour but leaving them unscathed everywhere else,[32] i.e., the eigenfunctions of $\hat{\tilde{H}}_\theta, \tilde{\varphi}_n(q)$, are identical to the eigenfunctions of $\hat{H}(q)$, $\varphi_{\varepsilon_n}(q)$, except on the complex contour, where the former are complex.

In this work, a simpler alternative for the definition of $\hat{\tilde{H}}$ is employed, which consists of adding an exterior optical potential to the Hamiltonian.[23,24] If such potential is constructed appropriately, its effects turn out to be equivalent to those of an exterior complex scaling. The explicit form of the optical potential is not required for the foregoing formal development and will be presented in Sec. IV.

The RTWPM (Ref. 22) for the determination of Hamiltonian eigenspectra requires the initial specification of a *test function*, whose spatial form is that of a wave packet. Such a function must satisfy the boundary conditions of the problem, otherwise being arbitrary at this point. Hence, if the development is carried out employing $\hat{\tilde{H}}$, a suitably chosen test function can be formally written as the linear superposition

$$\Psi(q) = \sum_n b_n \tilde{\varphi}_n(q), \qquad (6a)$$

where b_n is, in general, a complex number. On the other hand, if the development is carried out employing $\hat{H}$, any test function can also be formally expressed as the spectral expansion

$$\Psi(q) = \int c(\varepsilon) \varphi_\varepsilon(q) d\varepsilon, \qquad (6b)$$

where $c(\varepsilon)$ is, in general, a complex number as well. A procedure for the construction of a test function that satisfies Eqs. (6a) and (6b) simultaneously is presented in Sec. IV. Formal propagations in time of the expressions (6a) and (6b) with $\hat{\tilde{H}}$ and $\hat{H}$, respectively, yield

$$\tilde{\Psi}(q,t) = \sum_n b_n \tilde{\varphi}_n(q) \exp(-iE_n t/\hbar), \qquad (7a)$$

$$\Psi(q,t) = \int c(\varepsilon) \varphi_\varepsilon(q) \exp(-i\varepsilon t/\hbar) d\varepsilon. \qquad (7b)$$

For the determination of the resonance densities of states, first the propagated test function (7a) or (7b) is used to construct a *time-autocorrelation function*

$$\tilde{A}(t) := \langle \Psi(0)|\tilde{\Psi}(t)\rangle \qquad (8a)$$

$$= \sum_n |b_n|^2 \exp(-iE_n t/\hbar), \qquad (8b)$$

$$A(t) := \langle \Psi(0)|\Psi(t)\rangle \qquad (8c)$$

$$= \int |c(\varepsilon)|^2 \exp(-i\varepsilon/\hbar), \qquad (8d)$$

which is seen to measure the spatial overlap of the propagated test function with itself at the initial time. In order to obtain Eq. (8b), it is assumed that the $\tilde{\varphi}_n(q)$ are orthonormal. Although the wave functions (7a) and (7b) are different, since they are generated with different Hamiltonians, it can be guaranteed that the functions (8a) and (8c) turn out to be equal (see Sec. IV). Next, the truncated Fourier-Laplace transform of the time-autocorrelation function is evaluated in order to obtain the *spectral function*

$$\Omega_T(\varepsilon) := 2 \, \mathrm{Re}\left[\frac{1}{2\pi\hbar} \int_0^T A(t) \exp(i\varepsilon t/\hbar) dt\right] \qquad (9a)$$

$$\approx \sum_n |b_n|^2 L_n(\varepsilon - \varepsilon_n) \qquad (9b)$$

$$\approx |c(\varepsilon)|^2, \qquad (9c)$$

where $A(t) = \tilde{A}(t)$ is taken into account and Eqs. (8b) and (8d) are employed to obtain (9b) and (9c), respectively. Here, T is the total propagation time and $L_n(\varepsilon - \varepsilon_n)$ is the unit-area Lorentzian function

$$L_n(\varepsilon - \varepsilon_n) = \frac{1}{\pi} \frac{\Gamma_n/2}{(\varepsilon - \varepsilon_n)^2 + (\Gamma_n/2)^2}, \qquad (10)$$

whose FWHM is given by Γ_n. Equations (9b) and (9c) are obtained by assuming that T is long enough so that the effects of the convolution of the infinite-resolution spectral functions (9b) and (9c) with the unit-area line-shape function[22]

$$\delta_T(\varepsilon) := 2\,\mathrm{Re}\left[\frac{1}{2\pi\hbar}\int_0^T \exp(i\varepsilon t/\hbar)dt\right] \qquad (11a)$$

$$= \frac{\sin(\varepsilon T/\hbar)}{\pi\varepsilon} \qquad (11b)$$

$$\xrightarrow{T\to\infty} \delta(\varepsilon) \qquad (11c)$$

are negligible, i.e., so that the width of Eq. (11b) becomes much narrower than any of the resonance peaks. Equations (9b) and (9c) indicate that, for sufficiently long T, the calculated spectral function, employing either $\hat{\tilde{H}}$ or $\hat{H}$, consists of a series of Lorentzian (Breit-Wigner) resonances centered at the (real) peak eigenenergies, whose heights give the corresponding spectral weights by

$$|b_n|^2 \approx (\pi\Gamma_n/2)|c(\varepsilon_n)|^2 \approx (\pi\Gamma_n/2)\Omega_T(\varepsilon_n). \qquad (12)$$

Actually, since the resonance eigenfunctions $\tilde{\varphi}_n(q)$ are not necessarily orthonormal, the resonances may overlap and their line shapes may deviate from the Lorentzian profile. This would be a manifestation of the intrinsic nature of the spectrum and not of a limitation of the method. Finally, the normalized density of states associated with a given resonance is obtained by dividing the corresponding peak by its spectral weight (12).

Approximations to the resonance eigenfunctions of $\hat{\tilde{H}}$ are obtained from truncated Fourier-Laplace transforms, at the (real) peak energies, of any propagated test function (7a) [which needs not be the same as the one used in Eq. (8)],

$$\tilde{\Sigma}_T(q,\varepsilon_m) := 2\,\mathrm{Re}\left[\frac{1}{2\pi\hbar}\int_0^T \tilde{\Psi}(q,t)\exp(i\varepsilon_m t/\hbar)dt\right] \qquad (13a)$$

$$= \sum_n b_n \tilde{\varphi}_n(q) L_n(\varepsilon_n - \varepsilon_n) \qquad (13b)$$

$$\approx \frac{2}{\pi\Gamma_m} b_m \tilde{\varphi}_m(q), \qquad (13c)$$

where, in this case, it is assumed that b_n is a real number, i.e., that the test functions (6a) and (6b) are chosen real. Equation (13b) is obtained by assuming that T is long enough so that the effects of the convolution of the functions (10) and (11b) are negligible, and it is valid only in the region outside the support of the optical potential, where the $\tilde{\varphi}_n(q)$ are real, as indicated above. Furthermore, Eq. (13c) is obtained by assuming that the Lorentzians do not overlap strongly. It is observed that, for sufficiently long T and outside the optical potential, the real part of the Fourier component of the wave packet at the mth peak energy, $\tilde{\Sigma}_T(q,\varepsilon_m)$, yields an approximation to the corresponding complex-energy L^2 eigenfunction of $\hat{\tilde{H}}$ by

$$\tilde{\varphi}_m(q) \approx \frac{\pi\Gamma_m}{2b_m}\tilde{\Sigma}_T(q,\varepsilon_m). \qquad (14a)$$

These functions also provide L^2 approximations to the peak resonance eigenfunctions of $\hat{H}$ of uniform quality over a fi-

nite coordinate interval, whose length depends on how far in the asymptotic region the exterior optical potential is placed (see Secs. IV and V).

If the development is carried out with $\hat{H}$ instead, approximations to its peak resonance eigenfunctions are analogously obtained from truncated Fourier-Laplace transforms of any propagated test function (7b),

$$\Sigma_T(q,\varepsilon_m) := 2\,\mathrm{Re}\left[\frac{1}{2\pi\hbar}\int_0^T \Psi(q,t)\exp(i\varepsilon_m t/\hbar)dt\right] \qquad (13d)$$

$$= \int c(\varepsilon)\varphi_\varepsilon(q)\delta_T(\varepsilon_m - \varepsilon)d\varepsilon \qquad (13e)$$

$$\xrightarrow{T\to\infty} c(\varepsilon_m)\varphi_{\varepsilon_m}(q), \qquad (13f)$$

where $c(\varepsilon)$ is now assumed to be a real number too. It is observed that, for sufficiently long T, the real part of the Fourier component at the mth peak energy, $\Sigma_T(q,\varepsilon_m)$, yields an approximation to the corresponding eigenfunction by

$$\varphi_{\varepsilon_m}(q) \approx \frac{1}{c(\varepsilon_m)}\Sigma_T(q,\varepsilon_m). \qquad (14b)$$

Nevertheless, Eq. (13e) indicates that, no matter how long T becomes, $\Sigma_T(q,\varepsilon_m)$ actually constitutes a wave packet, since the convolution integral appearing there never collapses to a single term for finite T. Hence, the functions (14b) also constitute L^2 approximations to the peak resonance eigenfunctions of $\hat{H}$, of uniform quality over a finite coordinate interval, whose length, in this case, increases as T gets longer.[33] Employing Eq. (13e) it is readily verified that, for long enough T, the L^2 functions (14b) are approximately orthonormal, and that in the limit $T\to\infty$ they become Dirac-delta orthonormalized.

If the propagation time is long enough, the L^2 approximations (14a) and (14b) coincide everywhere, except in the region where the optical potential is located. This is due to the fact that such a potential, if constructed appropriately (Sec. IV), leaves the time-dependent wave function intact outside of that region, the same being true for the Fourier components (14a). The L^2 character of these approximations does not limit their practical applicability, since matrix elements involving continuum eigenfunctions, e.g., dipole matrix elements, converge at finite values of the integration limits. On the contrary, this method is conceptually appealing, since it avoids the practical use of the (unphysical) continuum eigenstates of $\hat{H}$, which are seen to play only an underlying formal role in this development.

The lifetime of a resonance is related to the imaginary part of its associated complex energy (2) by Eq. (5). According to Eq. (10), the most straightforward method, within the spectral definition, for determining the lifetime is to fit the calculated density of states to a Lorentzian function and to evaluate its FWHM.[9–15] Obviously, if the Lorentzian fit is

not precise, the lifetime obtained in this way is inaccurate. A method appropriate in this case consists of propagating the calculated resonance eigenfunction (14a) in time with $\hat{\bar{H}}$ [Eq. (3)] and calculating its squared norm [Eq. (4)]. Γ_n is then extracted from the slope of the logarithm of this function.[24] [Equivalently, the squared time-autocorrelation function $|\langle\bar{\Phi}_n(0)|\bar{\Phi}_n(t)\rangle|^2 = \exp(-\Gamma_n t/\hbar)$ can be employed].

IV. COMPUTATIONAL IMPLEMENTATION

The numerical integration of the TDSE, with the Hamiltonian (1) including the optical potential, was carried out by means of a finite-differences scheme, which is described in Refs. 22 and 28.

Since the computational grid is finite, with z_{min} and z_{max} its left- and right-hand boundaries, the artificial Dirichlet boundary conditions $\Psi(z_{min})=\Psi(z_{max})=0$ are imposed. Due to the shape of the potential (Fig. 1), the first condition is appropriate, provided z_{min} is far enough to the left from the well, which is easily accomplished. The second condition is appropriate only if the wave packet is never allowed to reach the boundary z_{max}; otherwise it would reflect from it giving rise to a spurious discretization of the continuum associated with the bound states of the computational box.[18] The most straightforward manner to avoid these problems, and also the most expensive, is simply to employ a large grid.[15,16] A more efficient approach, although still costly, is to allow the grid to expand in time along with the wave packet.[33] These two approaches would provide implementations of the RTWPM with the original Hamiltonian of the system, $\hat{H}$.

In this work, a much more efficient strategy is adopted, which afords an implementation of the RTWPM with the non-Hermitian Hamiltonian $\hat{\bar{H}}$ of Sec. III. The strategy relies on adding an optical potential with compact support,[23,24]

$$V_{opt}(z) = -i\,\gamma(z), \tag{15}$$

to $\hat{H}$ far to the right from the well. Since the modified Hamiltonian $\hat{\bar{H}}_\gamma \equiv \hat{H} + V_{opt}$ is not Hermitian, it causes the norm of the wave function to decrease in time as soon as it reaches the region where the optical potential is located. This can be used to advantage by tuning $\gamma(z)$ so as to completely damp the wave function in the asymptotic region before reaching the grid boundary, at the same time leaving it intact in the region of interest. The functional form

$$\gamma(z_0 \leq z \leq z_{max}) = \frac{\gamma_{max}}{2}\left[1 - \cos\frac{\pi(z-z_0)}{z_{max}-z_0}\right],$$

$$\gamma(z < z_0) = 0, \tag{16}$$

where γ_{max} is the maximum strength of $\gamma(z)$ and z_0 is the starting point of V_{opt}, is chosen since it has a continuous first derivative at $z = z_0$, consequently eliminating spurious reflections at that point.[33] Alternative techniques for the reflection-free simulation of the continuum that could be used in this context are exterior complex-coordinate contours,[32,34] coordinate stretching,[29] and infinite elements.[35]

Narrow real Gaussian wave packets located inside the well are used as test functions,[22] which are expected to be spectrally composed mainly of resonant states, since the relative amplitudes of resonant eigenfunctions are known to be much larger than the amplitudes of nonresonant ones in the well region. (If such Gaussians were located outside the well, the test function would mostly comprise nonresonant states). Hence, these functions are expected to satisfy Eq. (6a) with very good approximation, a claim that will be confirmed in the following section. Any contamination from nonresonant states in the test function would cause the spectral function (9b) to exhibit a background, which can be eliminated by propagating the test function with $\hat{\bar{H}}_\gamma$ for some time, prior to the evaluation of the time-autocorrelation function. This procedure is based on the observation that the exterior optical potential, besides serving as an asymptotic spatial absorber, also simultaneously acts as a filter of the nonresonant background comprised in the wave packet.[24] This can be understood by recognizing that the relative amplitudes of nonresonant eigenfunctions are larger than the amplitudes of resonant ones in the asymptotic region, causing the former to be damped more rapidly by the absorbing potential. This, in turn, is manifested by the fact that the lifetimes of the nonresonant eigenstates of $\hat{\bar{H}}_\gamma$ are much shorter than the lifetimes of its resonant ones.

In order to guarantee that the time-autocorrelation functions (8a) and (8c) turn out to be equal, it is sufficient to employ test functions (6a) and (6b) with compact support and to place the optical potential sufficiently far away from this region during the calculation of the time-autocorrelation function. This is justified by noticing that the initial and propagated test functions overlap only within the support region. Although, strictly speaking, a Gaussian does not possess compact support, in practice such a function vanishes beyond a certain point.

V. RESULTS AND DISCUSSION

A prototype system was first considered, consisting of an $Al_xGa_{1-x}As/GaAs/Al_xGa_{1-x}As$ rectangular QW of width $W = 200$ Å and barriers of height $V_0 = 336.7$ meV (which correspond to an Al concentration of $x = 0.45$ if a band offset of 0.6 is taken[36]). This rather wide structure was chosen in order to better illustrate the capabilities of the method, additional results for narrower QW's are reported below. The effective masses of the electron in the well and barrier regions were taken as $m_e^* = 0.0665 m_e$ and $m_e^* = 0.104 m_e$, respectively.[36] Calculations were performed for $F = 400$ and 1000 kV/cm, whose corresponding potential profiles are depicted in Fig. 1. Although these fields are relatively strong, they can be easily achieved experimentally. Appropriate grid and optical-potential parameters were found to be: $z_{min} = -300$ Å, $z_{max} = 650$ Å, $z_0 = 500$ Å, and $\gamma_{max} = 800$ meV. For the calculations with a position-independent effective mass, the barrier mass was also taken as $0.0665 m_e$.

The propagation times needed to obtain well-converged densities of states were $T = 8600$ and 140 fs, for 400 and 1000 kV/cm, respectively. The former took a much longer
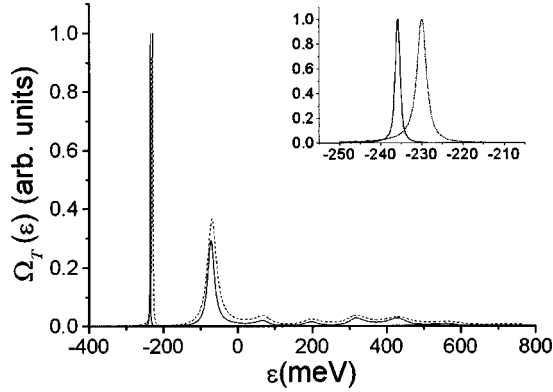
FIG. 2. Spectral function, displaying the weighted densities of states, calculated with a position-dependent (solid line) and a constant (dashed line) effective mass, for a $W = 200$ Å QW under $F = 400$ kV/cm. The inset shows an enlargement of the lowest-lying resonance.

FIG. 3. Spectral function, displaying the weighted densities of states, calculated with a position-dependent effective mass for a $W = 200$ Å QW under $F = 1000$ kV/cm.

time since the resonance widths are much smaller (see below). The filtering propagation was carried out for about 20 fs, until the norm of the initially unity-normalized real Gaussian wave packet decreased to ≈ 0.1. Spectral functions calculated with unfiltered and filtered test functions were observed to be very similar, confirming the expectation expressed in the preceding section.

In order to evaluate the Stark shifts, calculations were also performed for $F = 0$ kV/cm, employing the methodology described in Ref. 22. The field-free QW was found to support five bound states, with energies of 10.3, 43.5, 95.2, 166, and 256 meV, employing a position-dependent effective mass, and 11.0, 43.7, 96.3, 172, and 261 meV, employing a constant effective mass.

The solid curve of Fig. 2 displays the spectral function for $F = 400$ kV/cm, calculated employing a position-dependent effective mass. Out of the first five features observed, which likely correlate with the five field-free bound states, only the first two are tunneling resonances, since they lie below the barrier (see Fig. 1 and Table I), whereas the rest are remnants from above-barrier resonances. The inset shows an enlargement of the first resonance, which is seen to be very sharp compared to the second. Both tunneling resonances are found to fit very well to Lorentzian profiles. It must be kept in mind that their relative heights are proportional to their spectral weights (12), which, in turn, depend on the explicit
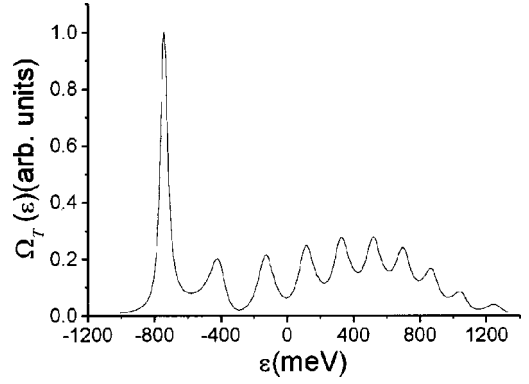
form of the test function employed for the calculation. However, the peak positions and FWHM's are independent of the test function employed, since these properties are intrinsic of the Hamiltonian. The negative Stark shifts are found to be very large (Table I).

Figure 3 displays the spectral function for $F = 1000$ kV/cm, calculated by employing a position-dependent effective mass. Due to the much stronger field, only one (broad) tunneling resonance (see Fig. 1 and Table I) and several overlapping above-barrier resonances are observed. Despite the overlap of the tunneling resonance with its neighbor, its line shape is still found to fit very well to a Lorentzian. As expected, the negative Stark shift is much larger than in the previous case (Table I).

The solid curves in Fig. 4 display three unity-normalized (L^2) eigenfunctions of $\hat{\bar{H}}_\gamma$ with $F = 400$ kV/cm, calculated with a position-dependent mass, corresponding to the two tunneling resonances and a nonresonant eigenstate in between them. These L^2 functions constitute good approximations to the eigenfunctions of $\hat{H}$ for $z < 500$ Å, at which point they are observed to be strongly damped by the optical potential. Since the first resonance is sharp, the lobe within the well exhibits a much larger amplitude than the outer oscillations, i.e., this state has a strong quasibound character. The relative amplitude of the outer oscillations of the second resonance is not so small, since this state is just below the barrier and presents a weaker bound character. The inner lobes of both resonance eigenfunctions are seen to be

TABLE I. Peak energies ($\varepsilon_n^{(F)}$), Stark shifts ($\Delta\varepsilon_n^{(F)} = \varepsilon_n^{(F)} - \varepsilon_n^{(0)}$), full widths at half maxima ($\Gamma_n^{(F)}$), and lifetimes ($\tau_n^{(F)}$) calculated with a constant (m^*) and position-dependent [$m^*(z)$] effective mass for a $W = 200$ Å QW under $F = 400$ and 1000 kV/cm.

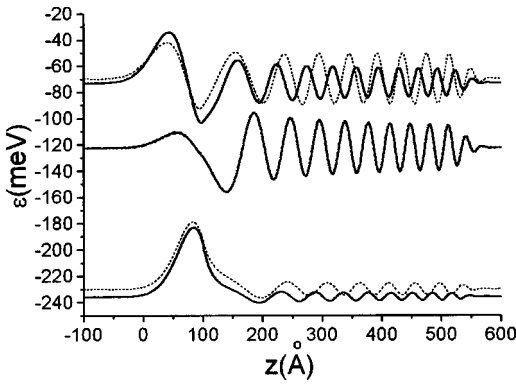|	$\varepsilon_n^{(F)}$ (meV)		$\Delta\varepsilon_n^{(F)}$ (meV)		$\Gamma_n^{(F)}$ (meV)		$\tau_n^{(F)}$ (fs)	
	m^*	$m^*(z)$	m^*	$m^*(z)$	m^*	$m^*(z)$	m^*	$m^*(z)$
			$W = 200$ Å, $F = 400$ kV/cm					
$n = 1$	-230	-236	-241	-246	2.48	0.895	264	735
$n = 2$	-70.9	-72.9	-114	-114	28.3	20.8	23.25	31.6
			$W = 200$ Å, $F = 1000$ kV/cm					
$n = 1$	-738	-743	-749	-753	70.7	48.1	9.30	13.6

FIG. 4. Peak resonance eigenfunctions, calculated with a position-dependent (solid lines) and a constant (dashed lines) effective mass, for a $W = 200$ Å QW under $F = 400$ kV/cm. A nonresonant eigenfunction with an intermediate energy, calculated with a position-dependent effective mass is also shown.

strongly pushed towards the lower edge of the well by the electric field. On the other hand, the nonresonant eigenfunction possesses a very small relative amplitude inside the well, an indication of the unbound character of this continuum state. The unity-normalized peak eigenfunction corresponding to the single tunneling resonance for $F = 1000$ kV/cm is shown in Fig. 5. As expected, this state presents much less bound character than in the previous case.

The upper and lower curves of Fig. 6 display the time-dependent norm and its logarithm (shifted up by 1), respectively, of the calculated eigenfunction corresponding to the $F = 400$ kV/cm first resonance peak (Figs. 2 and 4). The observed behavior is as predicted by Eq. (4), illustrating the validity of the norm method. In all cases, the FWHM and norm methods were found to yield the same lifetime values, which are reported in Table I. This agreement is due to the fact that the resonance profiles fitted well to Lorentzians and help to demonstrate the internal consistency of the methodology.

The dashed curve in Fig. 2 was calculated employing the constant effective mass. It is seen that this approximation induces relatively small spurious positive shifts in the resonance energies, but large underestimations of the tunneling lifetimes of up to about 300% (Table I). The dashed curves in
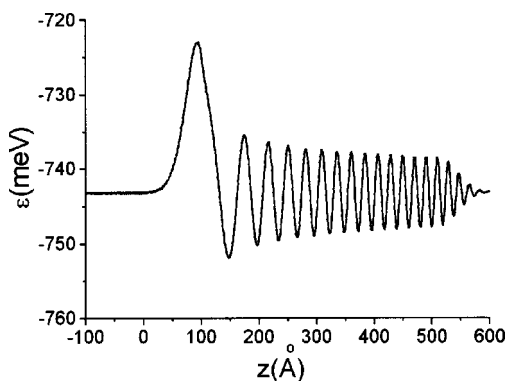

FIG. 5. Peak resonance eigenfunction, calculated with a position-dependent effective mass, for a $W = 200$ Å QW under $F = 400$ kV/cm.
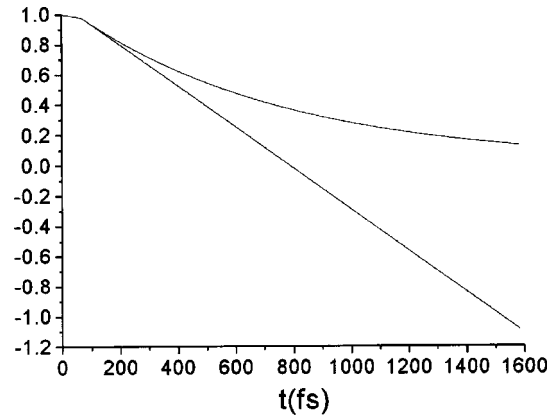

FIG. 6. Time-dependent norm (upper curve) and its logarithm (lower curve) of the lowest-lying resonance eigenfunction, calculated with a position-dependent effective mass, for a $W = 200$ Å QW under $F = 400$ kV/cm. The lower curve has been shifted up by 1.

Fig. 4 show the corresponding eigenfunctions, where the variations observed in the outer amplitudes are consistent with the decrease in the lifetimes. The underestimation of the lifetimes within the constant-mass approximation is easily understood by recalling that a light particle tunnels through a barrier more rapidly than a heavy one.[8] On the other hand, the reasons why this approximation causes positive energy shifts are not well understood yet.[8]

In order to compare the results of the RTWPM with available data from other approaches, calculations were also performed for narrower QW's under various field strengths. Table II displays the results, together with values taken from Refs. 10, 13, 15 and 16. For $W = 100$ Å and $F = 400$ kV/cm, the resonance energy and shift in the first row were calculated employing a numerical Fourier-series inverse-power (FIP) method,[15] whereas the lifetime was obtained by fitting the so-called tunneling probability (FTP), $P_1(t) = 1 - |\langle \varphi_1 | \varphi_1(t) \rangle|^2$, to the exponential function $1 - \exp(-\Gamma_1 t/\hbar)$ at long times, where $\varphi_1(t)$ is the *field-free* ground eigenfunction propagated in time with the Hamiltonian *including the dc field*.[15] The peak energy, shift, and FWHM in the second row were calculated by means of an Airy-function (AF) method.[15] (In Refs. 15 and 13, a slightly higher barrier of $V_0 = 340$ meV is employed). It is observed that, for energies, the FIP and AF methods agree fairly well with the RTWPM whereas, for lifetimes, the (constant-mass) FTP and (variable-mass) AF methods disagree with the RTWPM by almost three orders of magnitude, although they agree relatively well between them.

For $W = 100$ Å and $F = 250$ kV/cm, the peak energy and FWHM in the first and second rows were calculated employing Fourier-stabilization-graph (FSG) and AF methods, respectively.[15] The same properties in the third row were obtained by the same authors employing three different AF approaches.[13] For this field strength, the resonance is very sharp, requiring very long propagation times in order to converge the spectral function in the RTWPM. Therefore, only upper and lower bounds for the FWHM and lifetime, respectively, are reported. It is seen that the agreement between the FSG and AF methods of Ref. 15 is excellent, whereas the AF

TABLE II. Peak energies ($\varepsilon_n^{(F)}$), Stark shifts ($\Delta\varepsilon_n^{(F)} = \varepsilon_n^{(F)} - \varepsilon_n^{(0)}$), full widths at half maxima ($\Gamma_n^{(F)}$), and lifetimes ($\tau_n^{(F)}$) calculated with a constant (m^*) and a position-dependent [$m^*(z)$] effective mass for the indicated QW widths and field strengths.

	$\varepsilon^{(F)}$ (meV)		$\Delta\varepsilon^{(F)}$ (meV)		$\Gamma^{(F)}$ (meV)		$\tau^{(F)}$ (fs)	
	m^*	$m^*(z)$	m^*	$m^*(z)$	m^*	$m^*(z)$	m^*	$m^*(z)$
			$W=100$ Å, $F=400$ kV/cm					
FIP/TP[a]		-36.5		-70.16	5.22×10^{-3}		1.26×10^{5}	
AP[b]		-38.5		-72.2		3.03×10^{-3}		2.17×10^{5}
RTWPM	-34.3	-40.3	-68.8	-72.7	2.47	0.88	266	746
			$W=100$ Å, $F=250$ kV/cm					
FSG[c]		2.10		-31.6		1.24×10^{-6}		5.31×10^{8}
AF[b]		2.19		-31.5		1.26×10^{-6}		5.24×10^{8}
AF[d]		-0.94				0.145		4.54×10^{4}
RTWPM		-1.16		-33.5		<0.022		$>3.0\times10^{5}$
			$W=52$ Å, $F=200$ kV/cm					
FDIP/TP[e]		74.7		-5.2		2.63		2.5×10^{3}
RTWPM		74.5		-4.6		$<2.2\times10^{-2}$		$>3.0\times10^{5}$
			$W=30$ Å, $F=400$ kV/cm					
AF[f]			-11.2		7.31		900	
RTWPM	145	129	-18.0	-12.0	10.9	3.66	600	1800

[a]Reference 15. $V_0 = 340$ meV. Numerical Fourier-series inverse-power and tunneling-probability methods for the energy eigenvalues and lifetimes, respectively.

[b]Reference 15. Airy-function approach.

[c]Reference 15. Fourier-series stabilization-graph method.

[d]Reference 13. $V = 340$ meV. Airy-function approach.

[e]Reference 16. $W = 51$ Å, $V_0 = 300$ meV. Numerical finite-difference inverse-power and tunneling-probability methods for the energy eigenvalues and lifetimes, respectively. The values recorded are read off the reported curves.

[f]Reference 10. $V_0 = 400$ meV. Airy-function approach. The values recorded are read off the reported curves.

method from Ref. 13 provides a lower value of the resonance energy and a lifetime shorter by four orders of magnitude. In the latter reference, no comments are provided about the reasons for these disagreements. The RTWPM gives an even lower value for the resonance energy and a lifetime at least one order of magnitude longer than the AF method of Ref. 13.

For $W=52$ Å and $F=200$ kV/cm, the first row displays values read off from the curves reported in Ref. 16 (where a slightly smaller width of $W=51$ Å and a slightly lower barrier of $V_0=300$ meV are employed). In that work, the resonance energy and shift were calculated employing a numerical finite-difference-inverse-power (FDIP) method, whereas the lifetime was defined by the same fitting as in Ref. 15 (FDTP). For energies, the FDIP method is seen to agree very well with the RTWPM, however, the latter yields a lifetime longer by at least two orders of magnitude than the FDTP scheme.

Finally, for $W=30$ Å and $F=400$ kV/cm, the first row presents values extracted from the curves reported in Ref. 10, where the peak position and FWHM are obtained using an AF method. In that work, a constant mass and a barrier of $V_0=400$ meV are considered, which are expected to produce somewhat different values from the present work. With this

consideration in mind, it is observed that both the energy and the lifetime agree reasonably well with the RTWPM.

The lifetime values produced by the RTWPM and AF methods[10,13,15] are based on a spectral (static) definition [Eqs. (4) and (10)], whose physical interpretation has long been the object of controversy.[21] On the other hand, various explicitly time-dependent definitions of the lifetime[15,16,21] originate from appealing physical interpretations, but there is no reason to expect that they yield the same values as the spectral definition. In the particular case of the aforementioned TP fitting procedure,[15,16] this is due to the fact that an abrupt switching of the electric field leaves the electron in a spectrally wide nonstationary state,[37,38] with several resonance channels available for its escape from the well, resulting in a lifetime much shorter than that predicted by a static calculation. The spectral width of such a nonstationary state is manifested in transient oscillations of the time-autocorrelation function.[15,16,37–39] This explains, at least in part, the large discrepancy in the lifetime value between the FDTP method[16] and the RTWPM observed in Table II.

For the discrepancies in energy and lifetime values between the RTWPM and the FTP, AF, and FSG methods of Ref. 15, on the one hand, and the AF method of Ref. 13, on the other hand, the authors are unable to offer an explanation.

VI. CONCLUSIONS AND PERSPECTIVES

The present adaptation of the real-time wave-packet propagation method, by adding an optical (absorbing) potential to the Hamiltonian of the system in the asymptotic region, appears as an accurate and versatile numerical methodology for the calculation of continuum eigenspectra of low-dimensional semiconductor systems, in particular, resonance densities of states, lifetimes, and eigenfunctions. Its capability of producing the entire density of states in a single run and spectral lifetime values on the same footing makes it specially interesting. The method is also conceptually appealing, since no practical use is made of the (unphysical, non-L^2) eigenstates of the Hamiltonian, which play only an underlying formal role.

The strong resonance features (large Stark shifts and short mean lifetimes) exhibited by an electron in a quantum well under the field strengths considered in this work make this a convenient scenario for the study of the basic physics of the Stark effect, and may play an important role in the design of optoelectronic devices, such as modulators.

The closely related aspect of the dependence of the electron dynamics and the associated shake-up spectra on the strength and switching conditions of the applied field will be reported elsewhere. Work is also underway towards the extension of this methodology to the calculation of local densities of states and optical spectra within multiband models.

*Corresponding author. Electronic mail address: jarce@quimica.univalle.edu.co

[1] D. A. B. Miller, D. S. Chemla, T. D. Damen, A. C. Gossard, W. Weigmann, T. H. Wood, and C. A. Burrus, Phys. Rev. B **32**, 1043 (1985).

[2] C. Weisbuch and B. Vinter, *Quantum Semiconductor Structures* (Academic, Boston, 1991).

[3] L. Esaki, IEEE J. Quantum Electron. **QE-22**, 1611 (1986); A. Harwit and J. S. Harris, Appl. Phys. Lett. **50**, 685 (1987); B. F. Levine, K.-K. Choi, C. G. Bethea, J. Walker, and R. J. Malik, *ibid.* **50**, 1092 (1987).

[4] G. Bastard, E. E. Mendez, L. L. Chang, and L. Esaki, Phys. Rev. B **28**, 3241 (1983).

[5] G. Bastard and J. E. Brum, IEEE J. Quantum Electron. **QE-22**, 1625 (1986).

[6] M. Morita, K. Goro, and T. Suzuki, Jpn. J. Appl. Phys., Part 2 **29**, L1663 (1990).

[7] J. A. Kash, E. E. Mendez, and H. Morkoc, Appl. Phys. Lett. **46**, 173 (1985); B. F. Levine, J. Appl. Phys. **74**, R1 (1993).

[8] P. Harrison, *Quantum Wells, Wires, and Dots—Theoretical and Computational Physics* (Wiley, Chichester, 2000).

[9] D. Ahn and S. L. Chuang, Phys. Rev. B **34**, 9034 (1986); E. J. Austin and M. Jaros, *ibid.* **38**, 6326 (1988); D. M.-T. Kuo and Y. C. Chang, *ibid.* **60**, 15 957 (1999).

[10] G. Gonzáles de la Cruz, I. Delgadillo, and A. Calderón, Solid State Commun. **98**, 357 (1996).

[11] D. C. Hutchings, Appl. Phys. Lett. **55**, 1082 (1989).

[12] A. K. Ghatak, I. C. Goyal, and R. L. Gallawa, IEEE J. Quantum Electron. **26**, 305 (1990); S. Vatannia and G. Gildenblat, *ibid.* **32**, 1093 (1996).

[13] S. Panda and B. K. Panda, Pramana, J. Phys. **56**, 809 (2001).

[14] F. Borondo and J. Sánchez-Dehesa, Phys. Rev. B **33**, 8758 (1986); J. A. Proto, J. Sánchez-Dehesa, L. A. Cury, S. Nogare, and J. C. Portal, J. Phys.: Condens. Matter **6**, 887 (1994).

[15] S. Panda, B. K. Panda, and S. Fung, J. Phys.: Condens. Matter **11**, 5293 (1999).

[16] C. Juang, K. J. Kuhn, and R. B. Darling, Phys. Rev. B **41**, 12 047 (1990).

[17] S. Panda, B. K. Panda, S. Fung, and C. D. Beling, J. Appl. Phys. **80**, 1532 (1996).

[18] K. Nakamura, A. Shimizu, M. Koshiba, and K. Hayata, IEEE J. Quantum Electron. **25**, 889 (1989).

[19] M. Bylecki, W. Jaskolsky, and R. Oszwaldowsky, J. Phys.: Condens. Matter **8**, 6393 (1996).

[20] M. M. Vrubel, Semiconductors **28**, 35 (1994).

[21] R. Landauer and T. Martin, Rev. Mod. Phys. **66**, 217 (1994).

[22] D. F. Montaño, J. C. Arce, and N. Porras-Montenegro, J. Phys.: Condens. Matter **12**, 9917 (2000).

[23] R. Kosloff and D. Kosloff, J. Comput. Phys. **63**, 363 (1986); D. Neuhasuer and M. Baer, J. Chem. Phys. **90**, 4351 (1989).

[24] M. R. Hermann and J. A. Fleck, Jr., Phys. Rev. A **38**, 6000 (1988); A. Isele, C. Meier, V. Engel, N. Fahrer, and Ch. Schlier, J. Chem. Phys. **101**, 5919 (1994).

[25] N. A. Hill and K. B. Whaley, J. Chem. Phys. **99**, 3707 (1993).

[26] D. Hobbs, D. Weaire, S. McMurry, and O. Zuchuat, J. Phys.: Condens. Matter **8**, 4691 (1996).

[27] S. Nomura, T. Iitaka, X. Zhao, T. Sugano, and Y. Aoyagi, Phys. Rev. B **56**, R4348 (1997).

[28] S. Glutsch and D. S. Chemla, Phys. Rev. B **54**, 11 592 (1996).

[29] A. Ahland, D. Schulz, and E. Voges, Phys. Rev. B **60**, R5109 (1999).

[30] D. J. BenDaniel and C. B. Duke, Phys. Rev. **152**, 683 (1966); I. Galbraith and G. Duggan, Phys. Rev. B **38**, 10 057 (1988).

[31] J. Aguilar and J. Combes, Commun. Math. Phys. **22**, 269 (1971); E. Balslev and J. Combes, *ibid.* **22**, 280 (1971); B. Simon, *ibid.* **27**, 1 (1972).

[32] B. Simon, Phys. Lett. **71A**, 211 (1971).

[33] J. C. Arce, Ph.D. dissertation, Indiana University, 1992.

[34] C. W. McCurdy, C. K. Stroud, and M. Wisinsky, Phys. Rev. A **43**, 5980 (1991).

[35] J. J. Duque and J. C. Arce (unpublished).

[36] *Handbook Series on Semiconductor Parameters*, edited by M. Levinshtein, S. Rumyantsev, and M. Shur (World Scientific, Singapore, 1999), Vol. 2.

[37] M. L. Zambrano and J. C. Arce (unpublished).

[38] V. P. Oleinik and Ju. Arepiev, J. Phys. A **17**, 1817 (1984).

[39] R. Bluhm, A. Kostelecky, and B. Tudose, Phys. Rev. A **55**, 819 (1997).